

The Arizona Algorithm for Neutron-Star Lightcurve Modeling

Dimitrios Psaltis, Feryal Özel, Michi Bauböck, & Chi-kwan Chan

The text, figures, and results for this document were taken primarily from the following articles:

- Psaltis, D., Johannsen, T. 2012. A Ray-tracing Algorithm for Spinning Compact Object Spacetimes with Arbitrary Quadrupole Moments. I. Quasi-Kerr Black Holes. *The Astrophysical Journal* 745, 1
- Bauböck, M., Psaltis, D., Özel, F., Johannsen, T. 2012. A Ray-tracing Algorithm for Spinning Compact Object Spacetimes with Arbitrary Quadrupole Moments. II. Neutron Stars. *The Astrophysical Journal* 753, 175
- Chan, C.-k., Psaltis, D., Özel, F. 2013. GRay: A Massively Parallel GPU-based Code for Ray Tracing in Relativistic Spacetimes. *The Astrophysical Journal* 777, 13
- Bauböck, M., Berti, E., Psaltis, D., Özel, F. 2013. Relations between Neutron-star Parameters in the Hartle-Thorne Approximation. *The Astrophysical Journal* 777, 68
- Psaltis, D., Özel, F. 2014. Pulse Profiles from Spinning Neutron Stars in the Hartle-Thorne Approximation. *The Astrophysical Journal* 792, 87

Contents

1	Summary	3
2	The Neutron Star Metric	4
2.1	Geodesic Equations and Conservations Laws	5
3	The Neutron Star Properties	8
3.1	The Spin Angular Momentum	8
3.2	The Quadrupole Moment	9
3.3	The Stellar Surface	10
3.4	Summary	12
4	Numerical Integration of the Geodesic Equations	13
4.1	Treatment of the Coordinate Poles	13
5	The Observed Radiation Flux at Infinity	16
5.1	Discretization on the Image Plane	17
6	Convergence Tests And Code Performance	19
6.1	Performance	20

1 Summary

The Arizona algorithm integrates, at each rotational phase of the pulsar, the null geodesic equations from the two-dimensional image plane of a distant observer towards the stellar surface. It uses two Cartesian grids on the image plane: a coarse one, to find the approximate location of the hot spot as a function of pulse phase, and a smaller but finer one centered on the location of the hot spot, to integrate the specific intensity over the image plane and calculate the flux received by the observer.

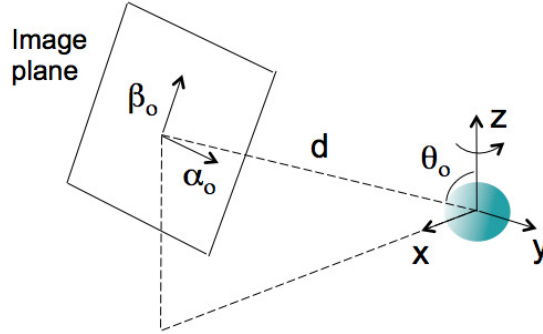


Figure 1: The geometry of the Arizona algorithm.

The metric of the spinning neutron star is that of Glampedakis & Babak (2006), which is the Kerr metric augmented by an additional quadrupole moment. At the limit of moderate spin frequencies, i.e., to second order in the neutron-star spin frequency, this metric reduces to the Hartle-Thorne metric (Hartle & Thorne 1968), which is the unique exterior metric of a spinning neutron star to the same order. For a given neutron star mass and radius, the spin angular momentum, the quadrupole moment, and the oblateness of the neutron-star surface are calculated using the empirical fitting formulae of Bauböck et al. (2013a).

In the following sections, we describe in detail the various elements of the algorithm.

2 The Neutron Star Metric

We describe the external spacetime of a rapidly spinning neutron star using the variant of the Hartle–Thorne metric developed by Glampedakis & Babak (2006).

We use Boyer–Lindquist coordinates and write the metric as

$$g_{\mu\nu} = g_{\mu\nu}^K + \eta a^2 h_{\mu\nu} . \quad (1)$$

Here $g_{\mu\nu}^K$ is the Kerr metric that corresponds to the line element

$$\begin{aligned} ds^2 = & - \left(1 - \frac{2Mr}{\Sigma}\right) dt^2 - \left(\frac{4Mar \sin^2 \theta}{\Sigma}\right) dt d\phi \\ & + \left(\frac{\Sigma}{\Delta}\right) dr^2 + \Sigma d\theta^2 \\ & + \left(r^2 + a^2 + \frac{2Ma^2 r \sin^2 \theta}{\Sigma}\right) \sin^2 \theta d\phi^2 \end{aligned} \quad (2)$$

with

$$\Delta \equiv r^2 - 2Mr + a^2 , \quad (3)$$

and

$$\Sigma \equiv r^2 + a^2 \cos^2 \theta . \quad (4)$$

The quadrupole correction is given, in contravariant form, by

$$\begin{aligned} h^{tt} &= (1 - 2M/r)^{-1} \left[(1 - 3 \cos^2 \theta) \mathcal{F}_1(r) \right] , \\ h^{rr} &= (1 - 2M/r) \left[(1 - 3 \cos^2 \theta) \mathcal{F}_1(r) \right] , \\ h^{\theta\theta} &= -\frac{1}{r^2} \left[(1 - 3 \cos^2 \theta) \mathcal{F}_2(r) \right] , \\ h^{\phi\phi} &= -\frac{1}{r^2 \sin^2 \theta} \left[(1 - 3 \cos^2 \theta) \mathcal{F}_2(r) \right] , \\ h^{t\phi} &= 0 , \end{aligned} \quad (5)$$

with the functions $\mathcal{F}_{1,2}(r)$ shown explicitly in Appendix A of Glampedakis & Babak (2006). In these equations and hereafter, we set $G = c = 1$. Note that, because it is of even order, the mass quadrupole affects only the diagonal components of the Kerr metric and not the $t\phi$ -component that measures the amount of frame dragging.

In this formulation, the spin of the neutron star is denoted by a and the quadrupole moment of the spacetime is

$$q = -(a^2 + \epsilon) = -a^2(1 + \eta) . \quad (6)$$

All the higher order moments take their corresponding Kerr values. In the last equation, we connect the formalism of Glampedakis & Babak (2006) to that of Laarakkers & Poisson (1999), for which $\epsilon = \eta a^2$. When $\eta = 0$, the metric reduces to the Kerr solution. When $a = 0$, the metric reduces to the Schwarzschild solution.

2.1 Geodesic Equations and Conservations Laws

We use metric (1) to integrate backwards in time the trajectories of individual photons from the image plane of an observer at infinity to the location of their emission. For the case of emission from the neutron star, the latter is the stellar surface. Following Cadeau et al. (2007), we use two integrals of motion to write first-order differential equations for the time coordinate and the azimuth of each photon trajectory. We then complete the system using the second-order differential equations for the geodesics along the radial and polar coordinates.

The metric (1) is stationary and axisymmetric. It is, therefore, characterized by the two usual Killing vectors, $\xi = (1, 0, 0, 0)$ and $\eta = (0, 0, 0, 1)$, which correspond to the conservation of energy

$$E = -g_{tt} \frac{dt}{d\lambda} - g_{t\phi} \frac{d\phi}{d\lambda} \quad (7)$$

and angular momentum

$$L = g_{\phi\phi} \frac{d\phi}{d\lambda} + g_{t\phi} \frac{dt}{d\lambda} \quad (8)$$

along the photon trajectory. Here, $g_{\mu\nu}$ is the $\mu\nu$ -element of the metric, and λ is an affine parameter. Using these two conserved quantities, we now write two first-order differential equations for the evolution of the t - and ϕ - components of the photon position as

$$\frac{dt}{d\lambda'} = \frac{-g_{\phi\phi} - b g_{t\phi}}{g_{\phi\phi} g_{tt} - g_{t\phi}^2} \quad (9)$$

and

$$\frac{d\phi}{d\lambda'} = \frac{b g_{tt} + g_{t\phi}}{g_{\phi\phi} g_{tt} - g_{t\phi}^2}. \quad (10)$$

where we have defined the normalized affine parameter $\lambda' \equiv E\lambda$ and the impact parameter for the photon trajectory $b \equiv L/E$.

For the r - and θ - components of the photon position we use the second-order geodesic equations, which for a general axisymmetric metric take the form

$$\frac{d^2 r}{d\lambda'^2} = -\Gamma_{tt}^r \left(\frac{dt}{d\lambda'} \right)^2 - \Gamma_{rr}^r \left(\frac{dr}{d\lambda'} \right)^2 - \Gamma_{\theta\theta}^r \left(\frac{d\theta}{d\lambda'} \right)^2 - \Gamma_{\phi\phi}^r \left(\frac{d\phi}{d\lambda'} \right)^2 - 2\Gamma_{\phi t}^r \left(\frac{d\phi}{d\lambda'} \right) \left(\frac{dt}{d\lambda'} \right) - 2\Gamma_{\theta r}^r \left(\frac{d\theta}{d\lambda'} \right) \left(\frac{dr}{d\lambda'} \right) \quad (11)$$

and

$$\frac{d^2 \theta}{d\lambda'^2} = -\Gamma_{tt}^\theta \left(\frac{dt}{d\lambda'} \right)^2 - \Gamma_{rr}^\theta \left(\frac{dr}{d\lambda'} \right)^2 - \Gamma_{\theta\theta}^\theta \left(\frac{d\theta}{d\lambda'} \right)^2 - \Gamma_{\phi\phi}^\theta \left(\frac{d\phi}{d\lambda'} \right)^2 - 2\Gamma_{\phi t}^\theta \left(\frac{d\phi}{d\lambda'} \right) \left(\frac{dt}{d\lambda'} \right) - 2\Gamma_{\theta r}^\theta \left(\frac{d\theta}{d\lambda'} \right) \left(\frac{dr}{d\lambda'} \right) \quad (12)$$

Here, $\Gamma_{\beta\gamma}^\alpha$ are the various Christoffel symbols for the metric (1).

A final integral of motion arises from the requirement that the norm of the photon 4-momentum has to vanish, i.e.,

$$g_{tt} \left(\frac{dt}{d\lambda'} \right)^2 + g_{rr} \left(\frac{dr}{d\lambda'} \right)^2 + g_{\theta\theta} \left(\frac{d\theta}{d\lambda'} \right)^2 + g_{\phi\phi} \left(\frac{d\phi}{d\lambda'} \right)^2 + 2g_{t\phi} \left(\frac{dt}{d\lambda'} \right) \left(\frac{d\phi}{d\lambda'} \right) = 0. \quad (13)$$

This integral of motion is not useful for replacing either the geodesic equation (11) or (12) because it contains the squares of the derivatives of the r - and θ - coordinates with respect to the affine parameter. Keeping track of the appropriate sign for the two derivatives, especially near the

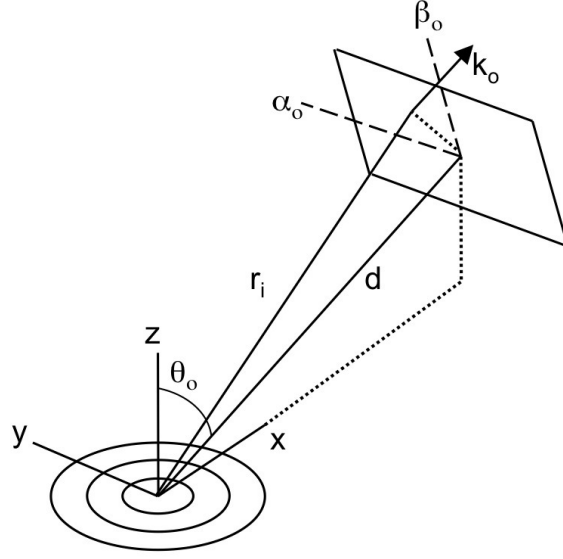


Figure 2: The two coordinate systems used in the geodesic integration.

inflection points of the geodesics, would more than offset the benefit of using a first-order integral of motion as opposed to a second-order geodesic equation. Therefore, following Cadeau et al. (2007), we use this integral of motion only in order to monitor the accuracy of the calculation. To this end, we define the parameter

$$\xi \equiv \left[g_{rr} \left(\frac{dr}{d\lambda'} \right)^2 + g_{\phi\phi} \left(\frac{d\phi}{d\lambda'} \right)^2 + g_{\theta\theta} \left(\frac{d\theta}{d\lambda'} \right)^2 + 2g_{t\phi} \left(\frac{dt}{d\lambda'} \right) \left(\frac{d\phi}{d\lambda'} \right) \right] / \left[g_{tt} \left(\frac{dt}{d\lambda'} \right)^2 \right] \quad (14)$$

and test whether its value remains equal to $\xi = -1$ along each geodesic.

In order to specify the initial conditions for the geodesic integration, we consider an observer viewing the neutron star from a large distance d and at an inclination angle θ_o from its rotation axis (see Fig. 2). We set up a virtual image plane that is perpendicular to the line of sight and centered at $\phi = 0$ of the spacetime.

We define the set of Cartesian coordinates (α_0, β_0) on the image plane such that the β_0 -axis is along the same fiducial plane and the α_0 -axis is perpendicular to it. We then convert the coordinates (α_0, β_0) of a photon that reaches the image plane to the coordinates (r_i, θ_i, ϕ_i) in the spherical-polar system used for the metric (1) with the relations (see Johannsen & Psaltis 2010)

$$r_i = \left(d^2 + \alpha_0^2 + \beta_0^2 \right)^{1/2} \quad (15)$$

$$\cos \theta_i = \frac{1}{r_i} (d \cos \theta_o + \beta_0 \sin \theta_o) \quad (16)$$

$$\tan \phi_i = \alpha_0 (d \sin \theta_o - \beta_0 \cos \theta_o)^{-1} . \quad (17)$$

The photons that contribute to the image of the compact object are those with 3-momenta that are perpendicular to the image plane. This orthogonality condition uniquely specifies the momentum vector of a photon with the above coordinates, according to the relations (Johannsen

& Psaltis 2010)

$$k^r \equiv \frac{dr}{d\lambda'} = \frac{d}{r_i} \quad (18)$$

$$k^\theta \equiv \frac{d\theta}{d\lambda'} = \left[-\cos \theta_o + \frac{d}{r_i^2} (d \cos \theta_o + \beta_0 \sin \theta_o) \right] \left[r_i^2 - (d \cos \theta_o + \beta_0 \sin \theta_o)^2 \right]^{-1/2} \quad (19)$$

$$k^\phi \equiv \frac{d\phi}{d\lambda'} = \frac{-\alpha_0 \sin \theta_o}{(d \sin \theta_o - \beta_0 \cos \theta_o)^2 + \alpha_0^2} . \quad (20)$$

Using these relations, we then calculate the t -component of the photon 4-momentum from equation (13). At this point, the normalization of the photon 4-momentum is arbitrary. Note that, for a distant observer, $d/r_i \rightarrow 1$, which implies that special care needs to be taken in evaluating expressions (19) and (20) to avoid round-off errors.

3 The Neutron Star Properties

The external spacetime of the neutron star is defined by four parameters: the mass M , the spin a and the quadrupole moment q . Moreover, the surface of the neutron star, assumed to be axisymmetric, is described by a function of the form $R = R(\theta)$. In Bauböck et al. (2013a), we devised a number of empirical relations that allow us to calculate the spin a , the quadrupole moment q , and the functional form of the stellar surface $R(\theta)$ in terms of the mass of the star M , the equatorial radius R_{eq} , and the spin frequency (as measured by an observer at infinity) f . We focused on the astrophysically relevant mass range of $M > 1M_{\odot}$ and on equations of state with a maximum mass that is $> 2M_{\odot}$.

Our expression will depend on the dimensionless ratio

$$\epsilon_0 = \frac{f}{f_0}, \quad (21)$$

where

$$f_0 \equiv \sqrt{\frac{GM_0}{R_0^3}}. \quad (22)$$

In this equation, M_0 and R_0 are the non-spinning mass and radius of the neutron star. The characteristic frequency f_0 corresponds to the Keplerian orbital period of a test particle at a radius R_0 around a mass M_0 and thus corresponds roughly to the maximum frequency a neutron star can be spun up to before breakup. For spin frequencies much smaller than this characteristic frequency ($f \ll f_0$), ϵ_0 serves as a suitable small parameter about which we can expand the metric. When f approaches f_0 , the parameter ϵ_0 approaches unity, and the HartleThorne approximation is no longer valid. The spin frequency at which this occurs depends on M_0 and R_0 and, therefore, on the equation of state. However, for most proposed equations of state, this approximation is valid for even the most rapidly spinning neutron stars observed to date (Berti et al. 2005).

In the following, we will also use the dimensionless compactness

$$\zeta = \frac{GM_0}{R_0 c^2}. \quad (23)$$

Note that both f_0 and ζ are written in terms of the mass and radius of the equivalent non-spinning star. However, since we are expanding all relevant quantities to the lowest order in ϵ_0 and the difference between the spinning and non-spinning mass and radius are already of second order in ϵ_0 , using the spinning mass and radius in the above expressions for f_0 and ζ will only contribute terms that are of higher order than the order of our approximation. In other words, we can use the mass and equatorial radius of a spinning neutron star to evaluate the characteristic frequency f_0 and the compactness ζ via equations (22) and (23).

3.1 The Spin Angular Momentum

The leading order term in the spin is linear in the small parameter ϵ_0 and we, therefore, write

$$a = \epsilon_0 a^*, \quad (24)$$

where a^* is a constant that depends, in principle, on the equation of state. In Bauböck et al. (2013a), we found the following approximate relation between this constant and the compactness of the neutron star

$$a^* = 1.1035 - 2.146\zeta + 4.5756\zeta^2. \quad (25)$$

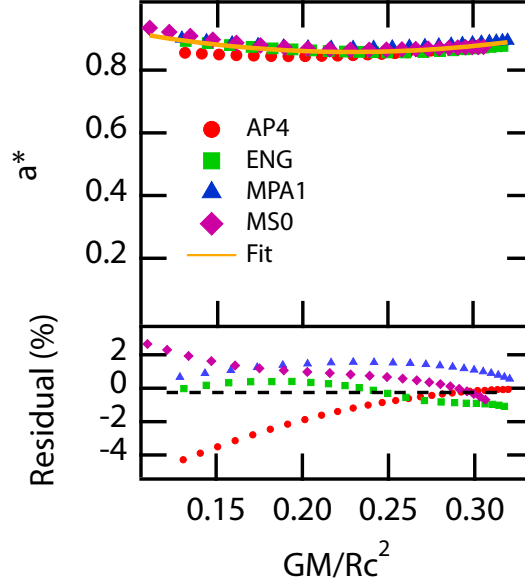


Figure 3: Empirical fit to the correlation between spin and compactness of a neutron star for four equations of state, corresponding to equation (25). The lower panel shows the residual in percent.

Figure 3 shows this fit as a solid line, along with the results of numerical calculations for four different equations of state. The lower panel shows the residuals; for all equations of state, the residuals over the range of masses considered here are less than 4%.

3.2 The Quadrupole Moment

To second order in the spin frequency, the neutron star acquires a quadrupole moment, i.e.,

$$q = \epsilon_0^2 q^*, \quad (26)$$

where again the constant q^* depends, in principle, on the equation of state.

In order to express the quantity q^* in terms of the macroscopic properties of the neutron star, we adopted, in Bauböck et al. (2013a), the relation proposed by Yagi & Yunes (2013) between the quadrupole moment and moment of inertia of spinning neutron stars with a variety of equations of state. They define a dimensionless quadrupole moment \bar{Q} and moment of inertia \bar{I} that relate to our q^* and a^* via

$$\bar{Q} \equiv \frac{q^*}{a^{*2}}, \quad (27)$$

and

$$\bar{I} \equiv a^* \zeta^{-3/2}. \quad (28)$$

They then find an empirical expression for \bar{I} as a function of \bar{Q} . Since the inverse of this relation is required for use with our fit for the spin parameter a^* in equation (25), we found instead an analogous fit for \bar{Q} as a function of \bar{I} ,

$$\begin{aligned} \ln \bar{Q} = & -2.014 + 0.601 \ln \bar{I} + 1.10 (\ln \bar{I})^2 \\ & - 0.412 (\ln \bar{I})^3 + 0.0459 (\ln \bar{I})^4. \end{aligned} \quad (29)$$

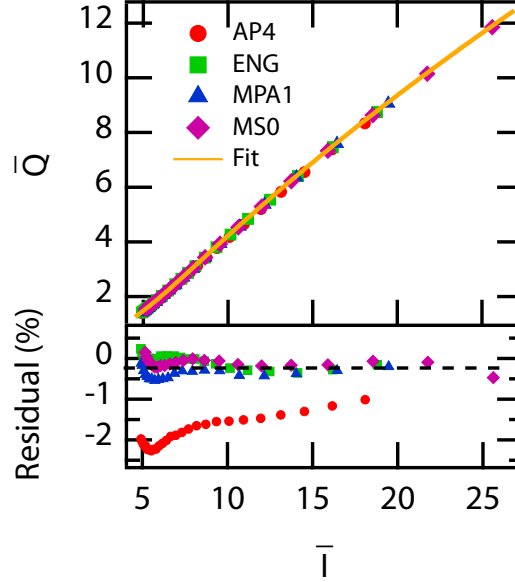


Figure 4: Empirical fit to the correlation between the dimensionless quadrupole moment \bar{Q} and angular momentum \bar{I} . The fit corresponds to Equation (29) and is equivalent to that proposed in Yagi & Yunes (2013). The lower panel shows the residual to the fit in percent.

The above fit is shown as the solid line in Figure 4 along with numerical calculations for our chosen equations of state. Again, the residuals shown in the lower panel are less than 2% for each considered equation of state.

3.3 The Stellar Surface

The surface of a spinning neutron star becomes oblate and, in the Hartle-Thorne approximation, this oblateness is described by an expression of the form

$$R(\theta) = R_0 + \xi_2 P_2(\cos \theta), \quad (30)$$

where P_2 is the second-order Legendre polynomial and ξ_2 is a coefficient depending on the equation of state and spin frequency of the neutron star. In the non-spinning limit, $\xi_2 = 0$ and $R(\theta) = R_0$. We will use a simpler form for this expression, i.e.,

$$R(\theta) = R_p + (R_{\text{eq}} - R_p) \cos^2 \theta, \quad (31)$$

where R_{eq} is the equatorial radius and R_p is the radius at the pole. Note that this expression is formally valid in Hartle-Thorne coordinates and not in the Boyer-Lindquist coordinates we use in our algorithm. In order to convert between the two, we use (Hartle & Thorne 1968; Glampedakis & Babak 2006)

$$\begin{aligned} R_{\text{BL}} &= R_{\text{HT}} - \frac{a^2}{2R_{\text{HT}}^3} \left[(R_{\text{HT}} + 2M)(R_{\text{HT}} - M) - \cos^2 \theta (R_{\text{HT}} - 2M)(R_{\text{HT}} + 3M) \right] \\ \theta_{\text{BL}} &= \theta_{\text{HT}} - \frac{a^2}{2R_{\text{HT}}^3} \sin \theta_{\text{BL}} \cos \theta_{\text{BL}} (R_{\text{HT}} + 2M), \end{aligned} \quad (32)$$

where the subscript “HT” refers to the Hartle-Thorne coordinate system and the subscript “BL” to the Boyer-Lindquist coordinate system. Also note that we describe a particular neutron-star configuration using the circumferential radius at the equator $R_{\text{eq},c}$, which is connected to the coordinate equatorial radius R_{eq} through the implicit equation

$$g_{\phi,\phi}(R_{\text{eq}}, \pi/2) = R_{\text{eq},c}^2. \quad (33)$$

For moderately spinning neutron stars, there are two frequently used parameters to characterize the oblate shape: the eccentricity of the surface,

$$e_s \equiv \sqrt{\left(\frac{R_{\text{eq}}}{R_p}\right)^2 - 1}, \quad (34)$$

and its ellipticity,

$$\varepsilon_s \equiv 1 - \frac{R_p}{R_{\text{eq}}}. \quad (35)$$

Equations (34) and (35) imply that the eccentricity of the surface of the neutron star has a first order dependence on the spin frequency

$$e_s = \epsilon_0 e_s^*, \quad (36)$$

while the ellipticity has a second-order dependence on the spin frequency, i.e.,

$$\varepsilon_s = \epsilon_0^2 \varepsilon_s^*. \quad (37)$$

Given the two empirical fits for the spin parameter and quadrupole moment, we derived in Bauböck et al. (2013a) an analytic expression for the eccentricity of the neutron star surface. Hartle & Thorne (1968) solved the equations of stellar structure at second order in spin frequency and showed that the eccentricity of the neutron star surface is given by

$$e_s = \sqrt{-3(v_2 - h_2 + \xi_2/R_0)}, \quad (38)$$

where v_2 and h_2 are functions of R_0 that are second order in spin, and ξ_2 is the parameter defined in Equation (30). Hartle & Thorne (1968) provide the exact forms of the quantities v_2 and h_2 as functions of the mass, radius, angular momentum, and quadrupole moment. In Bauböck et al. (2013a), we used these expressions to reduce equation (38) to depend only on the dimensionless parameters ζ , a , q , and ϵ_0 defined above, i.e.,

$$\begin{aligned} e_s^*(\zeta, a^*, q^*) = & \left[1 - 4a^* \zeta^{3/2} + \frac{15(a^{*2} - q^*)(3 - 6\zeta + 7\zeta^2)}{8\zeta^2} + \zeta^2 a^{*2} (3 + 4\zeta) \right. \\ & \left. + \frac{45}{16\zeta^2} (q^* - a^{*2})(\zeta - 1)(1 - 2\zeta + 2\zeta^2) \ln(1 - 2\zeta) \right]^{1/2}. \end{aligned} \quad (39)$$

Figure 5 shows this expression for the eccentricity as a function of the compactness, along with numerical calculations from several equations of state. We have substituted Equations (25), (28) and (29) into Equation (39) in order to present the relation as a function of the single parameter ζ . The residuals to this relation are shown in the lower panel. Even though we are using an exact analytic expression, the residuals are nonzero due to the empirical nature of the fits between a^* , q^* , and ζ .

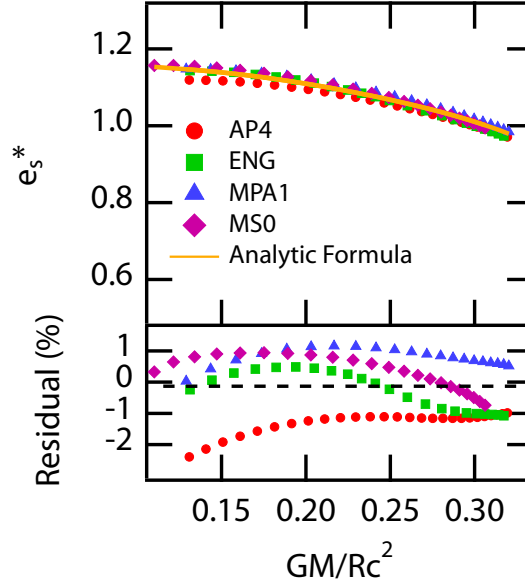


Figure 5: Analytic expression for the eccentricity of the neutron star surface, corresponding to Equation (39). In order to express this relation as a function of a single parameter, we have combined Equation (39) with our empirical fits for the quadrupole moment and spin parameter from Equations (25) and (29). The lower panel shows the residual to the relation in percent. Although the analytic relation is exact, the empirical fits between a^* , q^* , R , and M introduce some scatter about this relation.

3.4 Summary

In summary, we calculate all properties of the neutron-star surface and of its external metric given only three parameters. The neutron star mass M , its circumferential radius at the equator $R_{\text{eq},c}$, and its spin frequency f , as measured by an observer at infinity.

Using these three parameters, we calculate

1. the dimensionless ratio ϵ_0 using equations (21) and (22) and the compactness ζ using equation (23);
2. the spin angular momentum a using equations (24) and (25);
3. the moment of inertia of the neutron star \bar{I} using equation (28), the dimensionless quadrupole moment \bar{Q} using equation (29), the quadrupole constant q^* using equation (27), and finally the quadrupole moment q using equation (26);
4. the equatorial radius of the neutron star in Hartle-Thorne coordinates by solving numerically the implicit equation (33);
5. the eccentricity of the neutron-star surface e_s using equations (39) and (36);
6. the polar radius R_p using equation (34);
7. the neutron-star radius in Hartle-Thorne coordinates as a function of polar angle using equation (31);
8. the neutron-star radius in Boyer-Lindquist coordinates as a function of polar angle using equation (32).

4 Numerical Integration of the Geodesic Equations

We use a fourth order Runge-Kutta solver to integrate the four geodesic equations (9)-(12). A single geodesic is defined by its coordinates (α_0, β_0) on the image plane and is traced from the initial conditions (15)-(20) backward until it either intersect the surface of the star or its distance exceeds the distance between the observer and the star by 10%, at which point we assume that it has bypassed the star entirely.

In the Runge-Kutta solver, we employ an adaptive stepsize for the affine parameter λ' and we set it equal to a fixed fraction f of the inverse rate of the fastest changing variable at each point, i.e.,

$$\delta\lambda' = f \min \left[t \left(\frac{dt}{d\lambda'} \right)^{-1}, r \left(\frac{dr}{d\lambda'} \right)^{-1}, \theta \left(\frac{d\theta}{d\lambda'} \right)^{-1}, \phi \left(\frac{d\phi}{d\lambda'} \right)^{-1} \right]. \quad (40)$$

The above expression gives a zero stepsize at turning points of the geodesics, i.e., when one of the derivatives in the right-hand side becomes very large. For this reason, we set a minimum stepsize of $1/1024$.

Because the surface of the neutron star deviates from spherical symmetry at high spin frequencies and photons may intersect the surface at oblique angles, special care must be taken when evaluating the coordinates at which the photon geodesics intersect the stellar surface. We achieve this by repeating the last step in the integration of each geodesic while successively reducing its length by factors of 2 (i.e., using a bisection method) until the coordinate radius of the geodesic falls within a fractional distance ϵ_{NS} from the neutron-star radius at the same polar angle, i.e., until

$$\left| \frac{r(\theta) - R(\theta)}{R(\theta)} \right| \leq \epsilon_{\text{NS}}. \quad (41)$$

4.1 Treatment of the Coordinate Poles

The scheme described above can accurately integrate almost all geodesics. However, it breaks down for some of the geodesics that pass through the poles at $\theta = 0$ or π . To illustrate how the scheme breaks down, we choose the special initial conditions $r \cos \theta = 1000M$, $r \sin \theta = 4.833605M$, and $\phi = 0$ for which the photon trajectory passes both the south and north poles of a spin 0.99 black hole¹. In each panel of Figure 6, we plot the result of tracing the above ray with blue dotted lines.

In the left panel of Figure 6, the gray circle marks the location of the event horizon for the spin 0.99 black hole. The vertical black line is the pole. The green dashed and the red solid lines are the numerical trajectories of the photons with the same initial conditions but with different treatments of the coordinate singularity at the pole, as we will describe below. All three trajectories go around the south pole without any apparent problem and wind back to the north pole. While the red and green trajectories go through the north pole, circulate around the black hole a couple times, and eventually hit the event horizon, the blue trajectory is kicked back to infinity due to a numerical error.

The central panel of Figure 6 is a $100\times$ magnification of the region where the trajectories intersect with the north pole. It shows that the blue trajectory fails to step correctly across the pole. To pinpoint this numerical difficulty, we overplot all the Runge-Kutta sub- and full-steps by open and filled circles, respectively. The two overlapping open blue circles land very close to the pole.

¹Because of cylindrical symmetry, the value of ϕ is not important in this setup. Indeed, for $\phi = 0^\circ, 1^\circ, 2^\circ, \dots, 359^\circ$, the same pole problem is always encountered.

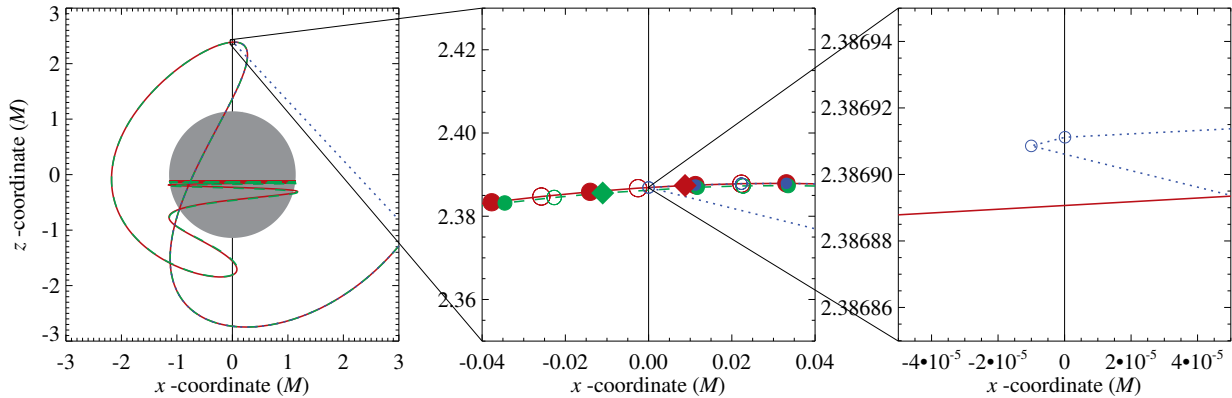


Figure 6: Numerical difficulties occur when the substeps of a 4th-order Runge-Kutta update is evaluated very close to, or on the two different sides, of the poles. In the left panel, the gray circle marks the location of the event horizon for a spin 0.99 black hole. The vertical black line is the coordinate pole. The red solid, green dashed, and blue dotted lines are numerical trajectories of the photons with the same initial conditions (see text) but with different treatments of the coordinate singularity at the pole. All three trajectories go around the south pole without any apparent problems and wind back to the north pole. However, while the red and green trajectories go through the north pole and eventually hit the event horizon, the blue trajectory is kicked back to infinity. The central panel zooms in by a factor of 100 to show that the blue trajectory fails to step across the pole. To understand this numerical problem, we overplot all the sub- and full-steps by open and filled circles, respectively. The two overlapping open blue circles are evaluated very close to the pole. The right panel zooms further in by another factor of 1000. It is now clear that the two open blue circles are located on different sides of the pole. The low-order truncation errors in the 4th-order Runge-Kutta scheme, instead of canceling, are enhanced. The green trajectory avoids this numerical problem by falling back to a 1st-order forward Euler scheme, marked by the green diamond in the central panel, whenever the geodesic moves across the pole. This 1st-order treatment has a larger truncation error because of the 1st-order stepping — this is visible in the central panel; and it may fail if a full step (filled circle) gets too close to the pole. To reduce the truncation error and make the integrator more robust, the red trajectory uses the forward Euler scheme with a smaller time step, which is marked by the red diamond in the central panel. The subsequent steps are all shifted to avoid the pole. This final treatment is what we employ in the production scheme.

The right panel offers a further $1000\times$ magnification of the same region. It is now clear that the two nearly overlapping open blue circles sit actually on the opposite sides of the pole. This is a problem for the 4th-order Runge-Kutta scheme, in which the solution is assumed to be smooth and can be Taylor expanded. In this scheme, the low-order truncation errors are normally canceled by a clever combination of the substeps. Evaluating the geodesic equation in the different substeps on the two sides of the pole, however, introduces an inconsistency in the scheme and enhances the low-order truncation errors.

The green trajectory in Figure 6 shows the result of an improved scheme, which solves the inconsistency by falling back to a 1st-order forward Euler step whenever a geodesic moves across the pole. The low-order step is marked by the green diamond in the central panel. This treatment mends the numerical difficulty and allows the photon to pass through the pole. Unfortunately, the low order stepping results in a larger truncation error in the numerical solution. The small but visible offset between the green trajectory and the other two trajectories in the central panel is indeed caused by the low order step at the south pole.

To reduce the truncation error of the low order step and make the integrator more robust, we monitor the quantity ξ (see, equation [14]), which should always remain equal to -1 . If $|\xi + 1| > \epsilon$, for some small parameter $\epsilon \sim 10^{-3}$ in the numerical scheme, we *re-integrate* the inaccurate step by falling back to the 1st-order forward Euler scheme with a *smaller* time step $\Delta\lambda'/9$. This step size is chosen so that (i) the absolute numerical error of the solution does not increase substantially

because of this single low-order step, and (ii) the pole is not encountered even if the Euler scheme is continuously applied. This 1st-order step is marked by the red diamond in the central panel of Figure 6. The subsequent steps, as shown in the figure by the red circles, are all shifted towards the left and skip the pole.

5 The Observed Radiation Flux at Infinity

The flux of radiation at photon energy E received on the image plane at time t is given by the integral

$$F_E(t) = \frac{1}{d^2} \int_{\alpha_0, \beta_0} I(\alpha_0, \beta_0; E, t) d\alpha_0 d\beta_0, \quad (42)$$

where $I(\alpha_0, \beta_0; E, t)$ is the specific intensity on the image plane of a point with coordinates (α_0, β_0) . Of all the photon rays that reach the image plane, only those that originate on the neutron-star surface have a non-zero intensity. Because of the strong gravitational field of the neutron star, these photon rays are not straight but are rather curved due to gravitational lensing.

The radii of all realistic neutron stars are larger than the radius of the photon orbit in their spacetimes. Under these conditions, photons arriving at position (α_0, β_0) on the image plane are uniquely connected to a position and direction on the stellar surface. As a result, we use the geodesic integrations to define a number of one-to-one maps between the coordinates (α_0, β_0) at which a photon ray crosses the image plane to various properties of the photons in their place of origin, i.e., the neutron-star surface. In particular, we use the five maps

$$\phi = \phi(\alpha_0, \beta_0) \quad (43)$$

$$\theta = \theta(\alpha_0, \beta_0) \quad (44)$$

$$t_d = t_d(\alpha_0, \beta_0), \quad (45)$$

$$\delta = \delta(\alpha_0, \beta_0) \quad (46)$$

$$\epsilon = \frac{1}{1+z} = \frac{E(\alpha_0, \beta_0)}{E_*(\phi, \theta)}. \quad (47)$$

The first three come directly from the geodesic integrations and connect the image-plane coordinates (α_0, β_0) of a photon ray to the longitude ϕ and latitude θ on the neutron star surface where the ray originates, as well as to the time of flight between the neutron star surface and the image plane.

We calculate the ratio ϵ (and the corresponding “redshift”) between the observed and emitted photon energies, E and E_* , using the properties of the time-like Killing vector, i.e.,

$$\epsilon = \frac{E}{E_*} = \frac{g_{\mu\nu, \text{im}}(\alpha_0, \beta_0) k_{\text{im}}^\mu(\alpha_0, \beta_0) u_{\text{im}}^\nu}{g_{\mu\nu, *}(\theta, \phi) k_*^\mu(\theta, \phi) u_*^\nu(\theta, \phi)}. \quad (48)$$

In this last expression, the subscripts “im” and “*” refer to the image plane and the stellar surface, respectively. We set the 3-velocity of the observer at the image plane to zero, i.e., we set $u_{\text{im}}^\nu = (1, 0, 0, 0)$ and the velocity of the observer at the stellar surface to

$$u_*^\nu = \frac{1}{\sqrt{-g_{tt} - \Omega(g_{\phi\phi}\Omega + 2g_{t\phi})}}(1, 0, 0, \Omega), \quad (49)$$

where $\Omega = 2\pi f$. This last expression comes from the requirement that the angular frequency of the neutron star, as measured by an observer at infinity, is equal to Ω .

Following Cadeau et al. (2007), we calculate the beaming angle δ at the point of intersection of the photon trajectory with the surface of the neutron star using the expression

$$\cos \delta = \frac{\sqrt{g^{rr}}}{1+z} \frac{k^r - k^\theta R'(\theta)}{\sqrt{1 + [R'(\theta)/R(\theta)]^2}}, \quad (50)$$

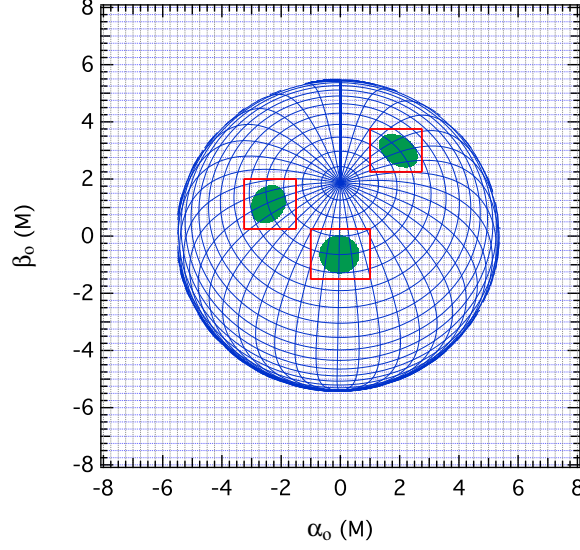


Figure 7: An illustration of the two grids used in a typical calculation of a lightcurve from a spinning neutron star. The image plane has a size of $16GM/c^2$ on which we have set up (for clarity) a 65×65 grid. Contours of constant latitude and longitude are shown in 10° intervals on the neutron star surface. A 10° hot spot on the neutron star is shown at a colatitude of 40° and at three different rotational phases: $\omega t = 0, \pi/2$, and $2\pi/3$. The red rectangles outline the regions in the low-resolution grid within which we set up a high-resolution grid, for each rotational phase. In this figure, the inclination of the observer is 30° , the neutron star has a mass of $1.8 M_\odot$, a radius of 10 km, other parameters that are typical of the FPS equation of state, and is spinning at 600 Hz in the clockwise direction.

where k^r and k^θ are the components of the photon momentum at the point of intersection with the stellar surface, $R(\theta)$ is the functional form of the surface of the neutron star (in Boyer-Lindquist coordinates), and $R'(\theta)$ is the derivative of this form with respect to the polar angle θ .

Because of the Lorentz invariance of the photon occupation number along a photon ray, we can now relate the specific intensity $I(\alpha_0, \beta_0; E, t)$ on the image plane to the specific intensity $I_{\text{NS}}(\theta, \phi, \delta; E, t)$ on the neutron star surface as

$$I(\alpha_0, \beta_0; E, t) = \epsilon^3 I_{\text{NS}}[\phi(\alpha_0, \beta_0), \theta(\alpha_0, \beta_0), \delta(\alpha_0, \beta_0); \frac{E}{\epsilon}, t - t_d(\alpha_0, \beta_0)] . \quad (51)$$

Inserting this last expression into equation (42) leads to an integral expression for the time- and energy-dependent radiation flux that flows through the image plane.

5.1 Discretization on the Image Plane

In order to calculate efficiently the flux of radiation through the image plane, especially when the size of the emitting region is very small, we evaluate the integral (42) using a set of two nested grids, as shown in Figure 7. We initially use the ray-tracing algorithm to calculate and store two of the mapping relations (43)-(47) on a low-resolution grid of $N_l \times N_l$ points, with a typical value of $N_l = 385$. For each rotational phase of the neutron star, we use these results in order to outline a rectangular region in the low-resolution grid that surrounds (within 5 degrees) the projection of

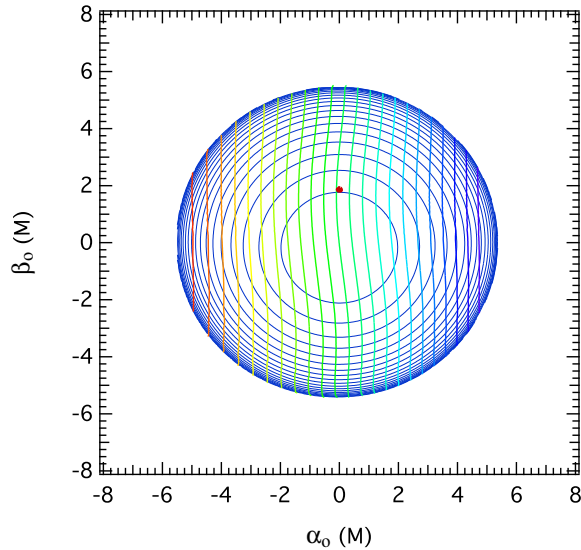


Figure 8: Contours of constant (*blue curves*) time delay and (*rainbow curves*) ratio of observed to emitted photon energy from the neutron star shown in Figure 7. The time-delay contours are at equidistant intervals in the range $(0.5 - 10) \times GM/c^2$; the photon-energy contours are at equidistant intervals in the range $0.62 - 0.74$. The red dot marks the location of the north rotational pole of the neutron star.

the emitting region on the image plane (shown as red rectangles in Figure 7 for three rotational phases). We then set up a high-resolution grid within each of these rectangular regions of $N_h \times N_h$ points, with a typical value of $N_h = 512$. Finally, we use the ray-tracing algorithm to calculate the mapping relations on the high-resolution grid and evaluate numerically the integral (42) only within this grid using a 2D trapezoid integration.

Attaining a sufficiently high resolution for the first two mapping relations (43)-(44) is what drives the requirement for a high-resolution grid. This is shown in Figure 7, where contours of constant latitude and longitude on the neutron star surface (in intervals of 10° , which is the same magnitude as the angular size of the spot in this example) are projected on the image plane. The separation of nearby contours decreases rapidly from the center of the stellar image to its edge; therefore, the number of image plane points falling within a spot near the edges also declines rapidly. The outline of even a large spot of an angular radius of 10° , as in this example, would be barely resolvable in the low-resolution grid shown in the figure as the spot makes its way towards the edge of the stellar image. In contrast, the last three mapping relations can be well approximated even on the low-resolution grid (even though we use the high-resolution grid for all calculations). This is shown in Figure 8, in which contours of constant energy ratios ϵ and time delays t_d are plotted on the image plane. As expected, the contours of constant redshift are nearly vertical curves spanning a narrow range, whereas the contours of constant time delay are nearly concentric circles, centered at the origin of the α_0, β_0 plane. In more detail, the waviness of the redshift contours arises from two competing effects: the frame-dragging correction to the magnitude of the surface velocity as measured by a zero-angular-momentum observer and the quadrupole correction to the gravitational redshift. Note that the redshift contours are further distorted and develop the island and saddle shapes shown, e.g., in the right panel of Figure 5 of Bauböck et al. (2013b), when the neutron star is viewed from a smaller inclination angle and has a larger quadrupole moment. The frame-dragging and the quadrupole corrections to the time-delay contours are typically less than $1/1000$ of the neutron star spin period and are, therefore, negligible.

6 Convergence Tests And Code Performance

The numerical accuracy of the Arizona algorithm depends on four aspects of the calculation. First is the distance d of the observer from the neutron star. Hereafter, we set $d = 10^5 M$ so that any residual gravitational redshift or divergence of the geodesics from being plane parallel is much smaller than the target level of 10^{-3} .

Second is the numerical accuracy of the integration of the individual null geodesics. This is done using a 4th order Runge-Kutta algorithm with an adaptive step in the affine parameter. The adaptive step is set to a fraction f of the inverse rate of the fastest changing variable at each point. The accuracy of the geodesic integrator depends entirely on this fraction f and its effect becomes more prominent at the limit of very small spot sizes. Because of the order of the numerical method used, this integration (as measured per geodesic) converges as f^4 .

Figure 9 shows the results of a convergence test for a particular null geodesic from a distant observer to the equatorial plane of the coordinate system. For this test, we set the image plane at a distance of $1028M$ and at an inclination of 40° . We also assume a compact object with a Kerr metric and spin equal to $a/M = 0.5$ at the center of the coordinates. The Cartesian coordinates on the image plane of the particular trajectory we are following are $(\alpha_0, \beta_0) = (5, 0)$. The figure shows the results of two different convergence tests, one in which the stepsize is kept fixed at $\delta\lambda' = f$ and one in which the stepsize is adaptive, following equation (40). In the case of adaptive stepsize and even for the moderate value of $f = 1/16$, the fractional error per geodesic is $\leq 10^{-5}$. For this reason, we set $f = 1/16$ hereafter.

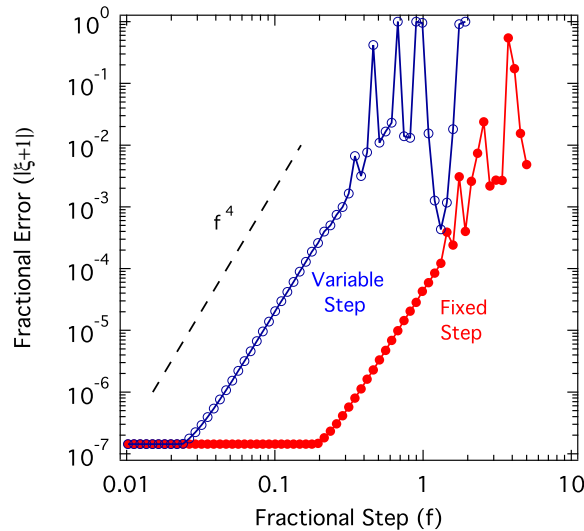


Figure 9: The fractional error introduced by the integration algorithm during the tracing of a single ray from the image plane to the equatorial plane, as a function of the fractional stepsize of the integration. The results of two integrations are shown, one with a fixed step in the affine parameter and one with a variable step. In both cases, the performance of the algorithm is consistent with the fourth-order of the integration method.

Third is the accuracy at which each null geodesic reaches the stellar surface. As discussed earlier, we achieve this by adaptively changing the last step in the integration of each geodesic until the coordinate radius reaches within a fractional distance of $\epsilon_{\text{NS}} = 10^{-5}$ of the neutron-star radius at that location. This ensures that any errors in the calculation of the gravitational redshift or of the solid angle of the emitting region is smaller than the target accuracy.

Finally, the numerical integration of the specific intensity on the observer’s image plane is done using a two-dimensional trapezoid algorithm, which has a nominal quadratic convergence. However, the accuracy of this integration is limited by the ability of the Cartesian grid on the image plane to accurately account for the shape of the gravitationally lensed hot spot on the surface of the neutron star. As a result, if N_h is the number of grid points along each of the directions on the fine grid, the convergence of this integration scales as $\sim N_h^{-1.5}$ (see Figure 4 of Psaltis & Özel 2014). It is also easy to see that configurations with large hot-spot sizes require more grid points on the fine grid than those with small hot-spot sizes.

In order to identify the optimal number of grid points on the image plane N_h for the configurations that are relevant to the NICER project, we performed the convergence test shown in Figure 10. We calculated the flux at 128 phase bins of a neutron star with a mass of $1.4M_\odot$ and a radius of 12 km, with a Schwarzschild metric but spinning at 200 Hz. The neutron-star surface has a hot spot of at a colatitude of 90° emitting as a blackbody at a temperature of 0.35 keV. The flux is calculated for an observer at the stellar equator and evaluated at a photon energy of 1 keV.

This test involves a very large hot spot and is, therefore, more sensitive to the number of grid points N_h on the image plane. The figure shows the r.m.s. and the max fractional errors between the lightcurves calculated with different numbers of grid points N_h and a fiducial, high resolution calculation that corresponds to $N_h = 512$. A value of $N_h = 256$ makes the r.m.s. errors to be less than our target accuracy of 10^{-3} for this particular test. In order to be conservative, we choose $N_h = 512$ for all the calculations performed hereafter.

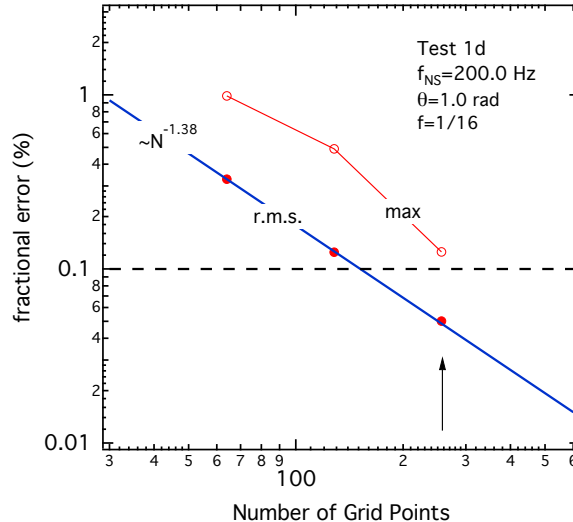


Figure 10: Convergence test for the numerical parameter that primarily affects the accuracy of the output of the Arizona algorithm. This figure shows the fractional error in the calculation of a lightcurve as a function of the number N_h of Cartesian grid points along each direction on the fine grid on the observer’s image plane. The maximum and the r.m.s. errors across the rotational phase are shown. The horizontal dashed line shows the target accuracy and the vertical arrow corresponds to $N_h = 256$.

6.1 Performance

In order to evaluate the performance of our ray tracing algorithm, we compute the projection of a uniform Cartesian grid in the image plane onto the equatorial plane of a spinning black hole. This problem was carried out in Schnittman & Bertschinger (2004) and then used as a test case in

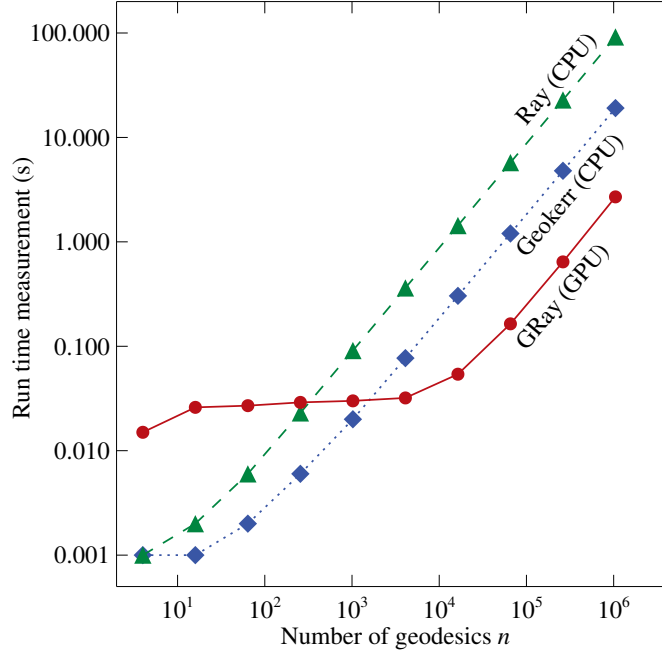


Figure 11: Run time measurements of the grid projection benchmark discussed in the text, using our algorithm running on CPUs (green triangles), our algorithm (GRay) running on GPUs (red circles) in double precision, and the publicly available algorithm **Geokerr** (blue diamonds). The run time measurements were performed on a MacBook Pro and are plotted against the number of geodesics traced for each image. The asymptotic linear dependence seen for all three algorithms demonstrates explicitly that the ray tracing problem is highly parallelizable. For a small number of geodesics, the performance of the GPU algorithm flattens to a constant value (approximately 20 ms for the configuration used) because of the time required for launching the CUDA kernel.

Dexter & Agol (2009). In particular, we choose $a = 0.95$ and $\eta = 0$ for the spacetime parameters and an observer inclination angle of 60° .

Figure 11 shows run time measurements of this grid projection benchmark, using our algorithm running on CPUs (green triangles), our algorithm (GRay) running on GPUs (red circles) in double precision, and the publicly available algorithm **Geokerr** (blue diamonds; see Dexter & Agol 2009). For a large number of geodesics, the ray tracing problem is highly parallelizable, as expected, and the use of GPUs speeds up the calculation by 1-2 orders of magnitude.

As discussed earlier, for the calculation of a lightcurve from a spinning neutron star, we require a fine grid of 512×512 geodesics per phase bin. For a single GPU (and not for a GPU cluster), the ray tracing algorithm can integrate 512×512 geodesics in about 0.25 seconds. For $N_{\text{phase}} = 128$ phase bins, this amounts to about 32 seconds. Since the problem is highly parallelizable, we can predict the performance of the algorithm using the scaling

$$\text{RunTime} = 32 \left(\frac{N_h}{512} \right)^2 \left(\frac{N_{\text{phase}}}{128} \right) \left(\frac{1}{N_{\text{GPU}}} \right) \text{ s} . \quad (52)$$

The Arizona GPU cluster **ElGato** has 67 nodes with 2 NVIDIA GPUs per node. Using the entire cluster reduces the run time to about 0.25 seconds for the calculation of a fully energy-dependent lightcurve per neutron-star configuration.

References

- [1] Bauböck, M., Berti, E., Psaltis, D., & Özel, F. 2013a, *ApJ*, 777, 68
- [2] Bauböck, M., Psaltis, D., & Özel, F. 2013b, *ApJ*, 766, 87
- [3] Bauböck, M., Psaltis, D., Özel, F., & Johannsen, T. 2012, *ApJ*, 753, 175
- [4] Berti, E., White, F., Maniopolou, A., & Bruni, M. 2005, *MNRAS*, 358, 923
- [5] Cadeau, C., Morsink, S. M., Leahy, D., & Campbell, S. S. 2007, *ApJ*, 654, 458
- [6] Chan, C.-k., Psaltis, D., & Özel, F. 2013, *ApJ*, 777, 13
- [7] Dexter, J., & Agol, E. 2009, *ApJ*, 696, 1616
- [8] Glampedakis, K., & Babak, S. 2006, *Classical and Quantum Gravity*, 23, 4167
- [9] Hartle, J. B., & Thorne, K. S. 1968, *ApJ*, 153, 807
- [10] Johannsen, T., & Psaltis, D. 2010, *ApJ*, 718, 446
- [11] Laarakkers, W. G., & Poisson, E. 1999, *ApJ*, 512, 282
- [12] Psaltis, D., & Johannsen, T. 2012, *ApJ*, 745, 1
- [13] Psaltis, D., & Özel, F. 2014, *ApJ*, 792, 87
- [14] Schnittman, J. D., & Bertschinger, E. 2004, *ApJ*, 606, 1098
- [15] Yagi, K., & Yunes, N. 2013, *Phys. Rev. D*, 88, 023009